



CHORUS

This is the accepted manuscript made available via CHORUS. The article has been published as:

Single atomic layer allotrope of bismuth with rectangular symmetry

P. J. Kowalczyk, O. Mahapatra, M. Le Ster, S. A. Brown, G. Bian, X. Wang, and T.-C. Chiang

Phys. Rev. B **96**, 205434 — Published 27 November 2017

DOI: [10.1103/PhysRevB.96.205434](https://doi.org/10.1103/PhysRevB.96.205434)

1 **A single atomic layer allotrope of bismuth with rectangular**
2 **symmetry**

3 P.J. Kowalczyk*

4 *Department of Solid State Physics,*
5 *Faculty of Physics and Applied Informatics,*
6 *University of Lodz, 90-236 Lodz, Pomorska 149/153, Poland*

7 O. Mahapatra, M. Le Ster, and S.A. Brown[†]

8 *The MacDiarmid Institute for Advanced Materials and Nanotechnology,*
9 *Department of Physics and Astronomy, University of Canterbury,*
10 *Private Bag 4800, Christchurch 8140, New Zealand*

11 G. Bian

12 *Department of Physics and Astronomy,*
13 *University of Missouri, Columbia, MO 65201, USA*

14 X. Wang

15 *College of Science, Nanjing University of Science and Technology, Nanjing 210094, China*

16 T.-C. Chiang

17 *Department of Physics, University of Illinois at Urbana-Champaign,*
18 *1110 West Green Street, Urbana, Illinois 61801-3080, USA*

Abstract

We report the observation of a new allotrope of two dimensional bismuth. Our Scanning Tunneling Microscopy experiments show that the structure is clearly different than the previously synthesized allotropes β - and α -bismuthene. It has a rectangular symmetry similar to that of α -bismuthene, but is composed of a puckered single monolayer of Bi atoms (α -bismuthene is intrinsically a paired layer material similar to black phosphorous). Atomic resolution images and an observed moiré pattern show that the new allotrope has a significantly contracted surface unit cell. The electronic structure is dominated by high density of states at the Fermi level as measured using scanning tunneling spectroscopy (STS) and confirmed by calculations based on density functional theory (DFT) which reveal Dirac cones at three different points in the Brillouin zone.

19 The last few years have seen an intensification of the search for new two dimensional
 20 (2D) systems, driven by discoveries of a multitude of new materials and many new physics
 21 phenomena. The starting point for this search was the exfoliation of graphene¹ which is
 22 characterized by extraordinary mechanical, thermal and electrical properties²⁻⁴. More re-
 23 cently silicene³⁻⁵ and germanene^{3,4,6} - the silicon and germanium analogues of graphene
 24 - have been reported, as well as the germanium analogue of graphane (CH)^{3,4,7}. Exfoli-
 25 ation of many other 2D materials was also possible^{3,8}, including MoS₂⁹⁻¹¹, WS₂^{10,11} and
 26 other transition-metal dichalcogenides¹¹ which are of course all compounds, in contrast to
 27 the elemental 2D materials graphene, silicene and germanene. The other group of layered,
 28 elemental 2D materials that has been synthesized is located in the 15th group of the peri-
 29 odic table and includes phosphorene^{3,4,12,13}, black arsenic¹⁴, β -bismuthene (β -Bi)^{4,15,16} (see
 30 Fig. 1(a)) and α -bismuthene (α -Bi)^{4,16-19} (see Fig. 1(b)). In fact many other group 15 2D
 31 structures have also been proposed, including the δ , ϵ , ζ , η , θ and ι forms of phosphorene,
 32 arsenene, antimonene and bismuthene^{16,20}.

33 β -Bi is a hexagonal (111) structure (A7 crystallographic structure) that grows as a sin-
 34 gle monolayer [the confusing terminology 'bilayer' is sometimes used to indicate that the
 35 monolayer actually comprises atoms in two distinct sites, at different heights, as shown in
 36 Fig. 1(a)]. In contrast, phosphorene and α -Bi have the black phosphorus like (BP-like) A17
 37 structure (Fig. 1(b)). These crystallise in the (110) orientation, with a rectangular unit cell
 38 and are *intrinsically paired* layer structures comprising *two* atomic layers that are connected
 39 by strong interlayer bonds. Both Bi(111) and Bi(110) structures are of high importance
 40 because their edges may support topologically protected edge states^{21,22}.

41 The structure shown in Fig. 1(b) makes it clear that a single monolayer of the A17
 42 structure is not possible because the second layer is *required* to bind it together: the A17
 43 structure can *only* exist in paired layer form. Nevertheless, in this Letter we provide evidence
 44 for a never previously reported 2D allotrope of monolayer bismuth (MBi) with rectangular
 45 symmetry similar to that of the Bi(110) structure shown in Fig. 1(b), but with a substantially
 46 contracted surface unit cell (see Fig. 1(c)). The MBi is physisorbed on top of α -Bi^{18,19}.
 47 Our experimental STM/STS results are supported by DFT calculations which identify the
 48 minimum energy structure and show that the contracted Bi(110) unit cell is achieved through
 49 strong puckering i.e. out-of-plane distortion of the rectangular unit cell.

50 Commercially available HOPG (SPI-1) was used as a substrate in all experiments. It was

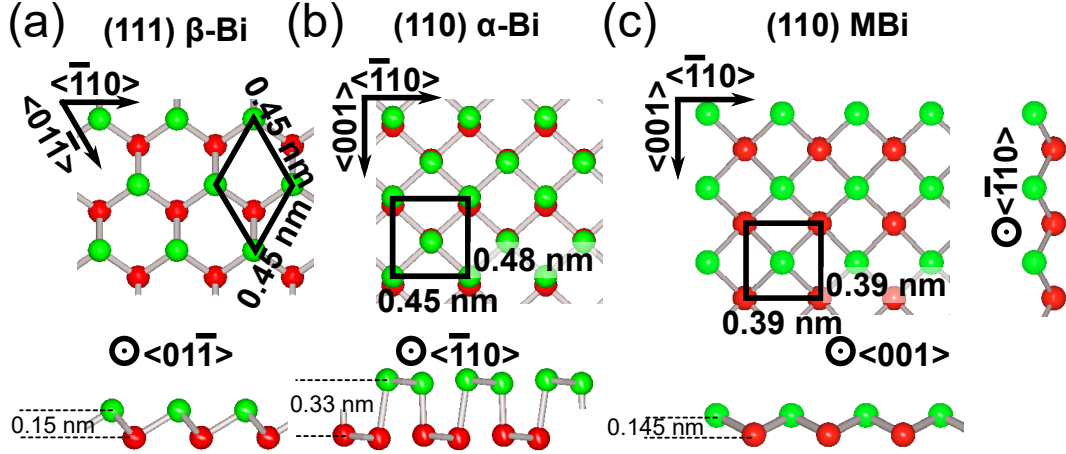


FIG. 1. Crystallographic structure of Bismuth allotropes: (a) β -Bi (hexagonal, (111) structure), (b) α -Bi ((110) paired layer structure with rectangular unit cell) and (c) monolayer bismuth (MBi) - the new single layer rectangular structure reported here. Crystallographic directions, unit cells and interlayer distances are marked in each case.

51 cleaved in air, then loaded into the UHV system and annealed at 700 – 900 K for several
 52 hours to remove contaminants. After the substrate cooled down to room temperature, high
 53 purity bismuth (99.999%) was evaporated from a ceramic crucible and deposited onto the
 54 substrate at rates $\sim 0.01 \text{ \AA/s}$. The film thickness was monitored with a calibrated quartz
 55 crystal, and was measured in units of monolayers (ML). Here we define 1 ML as the thickness
 56 equivalent to that of a single rhombohedral Bi(110) plane i.e. 3.3 \AA^{23} .

57 STM measurements were carried out using an Omicron UHV STM at a base pressure
 58 of 10^{-8} Pa at 50 K (LT) and room temperature (300 K), using cut Pt90%-Ir10% tips.
 59 Typical scanning parameters used during measurements were $V_{bias} = -0.8 \text{ V}$ and $I = 10 \text{ pA}$.
 60 STS measurements ($\pm 1.0 \text{ V}$, 128 points per curve) were done in current imaging tunneling
 61 spectroscopy mode (CITS, $128 \times 128 \text{ pts}^2$). All STS/CITS measurements were done at low
 62 temperature (LT). Measurement and data analysis procedures are similar to those described
 63 in Ref. [19]; dI/dV was calculated numerically and the presented data are spatial averages
 64 of $\sim 100 dI/dV$ curves.

65 First-principles calculations of the electronic structure of freestanding MBi films were
 66 performed using Hartwigsen-Goedecker-Hutter-type (HGH) pseudopotentials and a plane-
 67 wave basis set, following methods discussed in detail previously^{24,25}. The main program
 68 employed was developed by the ABINIT group. Spin-orbit coupling was included using the

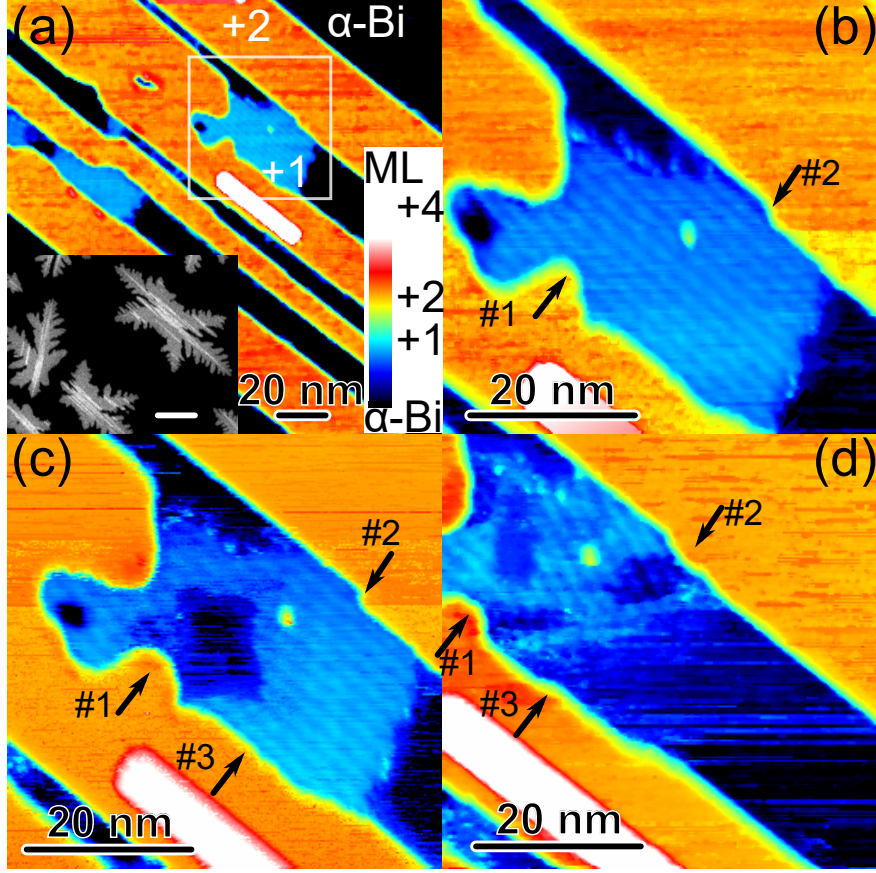


FIG. 2. (a) $150 \times 150 \text{ nm}^2$ RT STM image showing magnification of large star-like shaped Bi island (inset: SEM image showing typical star-shaped islands, scale bar corresponds to $1 \mu\text{m}$) with additional one monolayer thick MBI ad-layers (+1) grown on top of α -Bi base between stripes (+2). (b)-(d) Series of three $50 \times 50 \text{ nm}^2$ STM images recorded in the region indicated by the square in (a), showing STM modification of the MBI ad-layer. Arrows marked #1-3 show locations on the edges of the 2 ML stripes which changed during STM modification.

69 relativistic LDA approximation. Densities of states are calculated by integrating over the
70 entire Brillouin zone. The vacuum layer thickness was 2 nm and the unit cell dimensions
71 are discussed below.

72 The inset in Fig. 2(a) shows the typical morphology of the star-shaped Bi islands that
73 grow on flat terraces of the HOPG substrate. Previous work^{16-19,26-30} has shown that these
74 islands have the α -Bi structure and a morphology which is characterized by large atomically
75 flat island bases on top of which additional 2 ML high stripes are formed^{26,28}. The stripes
76 are parallel to the $\langle \bar{1}10 \rangle$ direction of the α -Bi lattice. In this work we focus on unusual

77 single monolayer structures, identified here as MBi, which are occasionally found on the
78 α -Bi bases. One MBi structure is highlighted by the the box in Fig. 2 (a), and shown in
79 greater detail in Fig. 2 (b); other MBi structures can be observed to the left of the box
80 in Fig. 2 (a). The MBi structures have been observed many times, always between long
81 parallel 2ML α -Bi stripes. The lateral dimensions of the MBi are below 50 nm while their
82 STM measured heights are 0.2 ± 0.1 nm (measured from the base). Experimental issues
83 mean that it is difficult to measure the height more precisely but it is clearly different from
84 the surrounding 2 ML stripes which are 0.66 ± 0.01 nm high²⁸. In addition, a moiré pattern
85 can be observed on top of the MBi, with a modulation that is almost (but not quite) parallel
86 to the 2 ML stripes - this is discussed in detail below.

87 We find that MBi is always found in regions in which at least one of the neighbouring
88 stripes is defected (see Fig. 2(b), features labelled #1 and #2). Extensive previous studies of
89 the growth of bismuth islands and nanorods by diffusion and aggregation^{18,19,23,26-30} suggest
90 that the mechanism of MBi formation is that (i) Bi atoms land on the α -Bi surface during
91 the deposition process, (ii) the atoms diffuse in the region between the long stripes and (iii)
92 these freely diffusing atoms are pinned by a defect (e.g. a kink in the stripe) which results
93 in MBi nucleation.

94 In order to determine if the MBi is bonded to the underlying Bi atoms we used the STM
95 tip to induce modification of the structure. First we zoom in to a selected region of the
96 ad-layer (scan size 10×10 nm²) using the usual setpoint current (10 pA), and then increase
97 the set point current to 1 nA to reduce the tip-sample distance and increase the tip-sample
98 interaction. After performing a full scan we reduce the setpoint current to 10 pA and
99 enlarge the scan size in order to check if any morphological changes of the topography can
100 be observed. The results of this series of experiments is shown in Fig. 2(b)-(d). It is obvious
101 that this procedure causes modification of the ad-layer – holes reaching the underlying α -Bi
102 base are formed. Bi atoms initially located in the hole are often transferred to the stripes'
103 edges which results in a morphology change. For example, in Fig. 2 (b-d) the protusion
104 labelled #1 and the kink labelled #2 become rounded, and a new protrusion forms at #3.
105 Note that when similar experiments are performed away from the ad-layer no changes to
106 the bases and stripes are observed. These observations indicate that the observed ad-layer
107 is weakly bonded to the supporting α -Bi base. It is an open question whether support by
108 neighbouring stripes is required to stabilise the MBi film, or whether the stripes merely

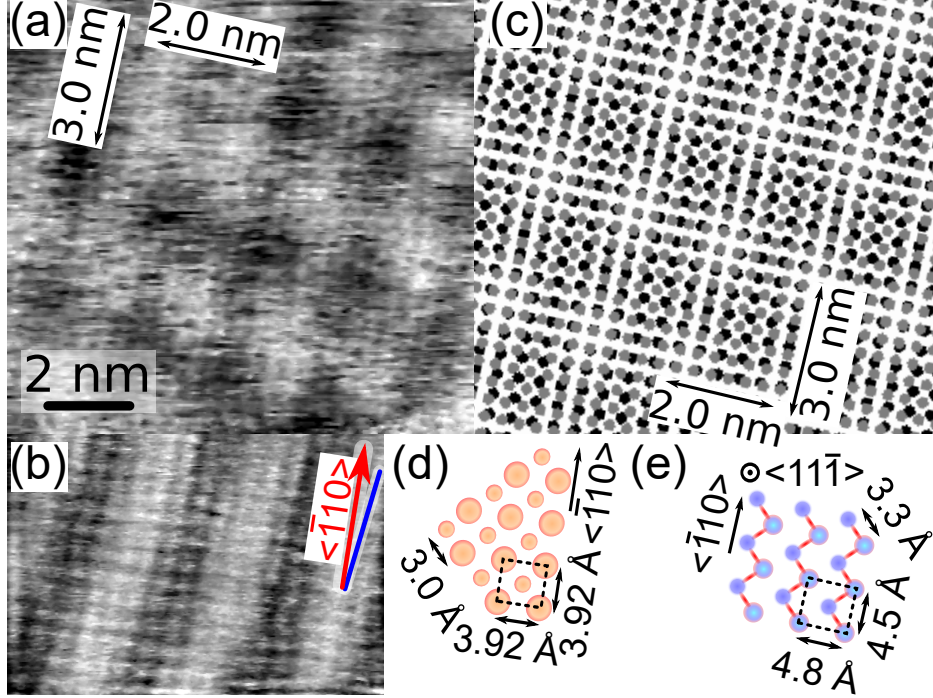


FIG. 3. (a) LT STM image (-0.8 V, 0.2 nA) showing clear moiré pattern recorded on MBI. (b) Further high resolution STM image with clear atomic resolution; Red and blue bars indicate the direction of overlayer atoms and moiré pattern respectively. (c) Moiré pattern simulation obtained by superposition of the two unit cells shown in (d) and (e). Only the corner atoms in each unit cell are shown because the puckering effect (see side views, Fig. 1) means that the other atom in the unit cell is in a different plane and not usually visible in the STM measurements. Periodicities of both moiré patterns are indicated in (a) and (c).

109 allow nucleation of the MBI, as described above.

110 The crystallographic structure of the MBI can be deduced from atomic resolution images.
 111 Figs. 3(a,b) clearly show a rectangularly arranged mesh of atoms which suggests strongly
 112 that we are dealing with a structure more similar to that of α -Bi [Bi(110)] than hexagonal
 113 β -Bi [Bi(111)]. The unit cell is estimated (from the atomic resolution images and fast Fourier
 114 transforms) to be $(0.40 \pm 0.02) \times (0.41 \pm 0.02) \text{ nm}^2$. These dimensions are much smaller
 115 than for bulk Bi(110) $(0.455 \times 0.475 \text{ nm}^2)^{31}$ and Bi(110) films on HOPG $(0.45 \pm 0.02 \times 0.48 \pm$
 116 $0.02 \text{ nm}^2)^{18,28-30}$, indicating an $\sim 10\%$ compression of the MBI unit cell with respect to the
 117 underlying α -Bi base.

118 This difference in unit cells of the MBI and α -Bi manifests itself also by formation of

119 a moiré pattern observed by STM as in Figs. 2(a)-(d) and 3(a,b) i.e. there is a periodic
 120 modulation of the apparent height in a direction nearly parallel to the 2 ML stripes (this is
 121 the Bi $\langle\bar{1}10\rangle$ direction²⁶). This additional modulation is more clearly visible in some images
 122 than others e.g. it is less clear in Fig. 3(b) than in Fig. 3(a). The moiré pattern periodicity
 123 is estimated to be ~ 2.0 nm and its orientation differs by $\sim 6^\circ$ with respect to the atomic
 124 rows i.e. to the $\langle\bar{1}10\rangle$ direction (see blue and red lines in Fig. 3(b)). Close inspection of
 125 Fig. 3(a) reveals that the intensity along each moiré stripe is additionally modulated with
 126 periodicity of ~ 3 nm. The angle between these two periodicities is estimated to $80^\circ \pm 10^\circ$.
 127 A further important feature of the data is that after modification the moiré pattern rotates
 128 by $\sim 20^\circ$ but does not change its period significantly.

129 We explain the experimental observations using a simple superposition model.³⁰ Fig. 3(c)
 130 shows the result of super-posing MBi with unit cell 0.392×0.392 nm² on α -Bi with unit
 131 cell 0.450×0.480 nm² (see Fig. 3(d) and (e) for ball models for the individual layers). This
 132 combination nicely reproduces the experimentally observed features: the moiré periodicities
 133 are ~ 2.0 and ~ 3.0 nm as in Fig. 3(a), the angle between them is 78° , and the angle between
 134 the atomic rows and the moiré pattern is 4° . Additionally (see Fig. S1 in supplementary
 135 materials), on rotation of the MBi layer by 4° with respect to the α -Bi layer we find that
 136 the period of the moiré pattern is unchanged even though its angle with respect to the
 137 Bi $\langle\bar{1}10\rangle$ direction changes by $\sim 20^\circ$, as is observed experimentally (Fig. 2(c) and (d)). This
 138 (lack of) angular dependence, along with an exquisite sensitivity of the moiré periodicity to
 139 changes in the MBi unit cell (see Fig. S1), allows a much more precise determination of the
 140 MBi lattice parameter than the atomic resolution images in Fig. 2 i.e. 0.39 nm, with an
 141 uncertainty smaller than 0.01 nm.³²

142 In Fig. 4(a) we show results of our STS experiments. dI/dV curves #1 and #2 were
 143 recorded on the α -Bi base and MBi respectively. In the ± 1 eV range the local density
 144 of states for the α -Bi is characterized by two distinct peaks located at ~ -0.3 eV and
 145 $\sim +0.5$ eV.¹⁹ The dI/dV curve for the MBi (#2) is characterized by the presence of three
 146 maxima located at -0.1 eV, $+0.1$ eV, and $+0.4$ eV.

147 To understand the electronic structure of the MBi we have performed DFT calculations
 148 to determine the minimum energy structures and also to investigate the band structure.
 149 A $17 \times 17 \times 1$ sampling grid in momentum space was employed in accordance with the
 150 Monkhorst-Pack method and the cutoff of electron kinetic energy was set to 400 eV. The

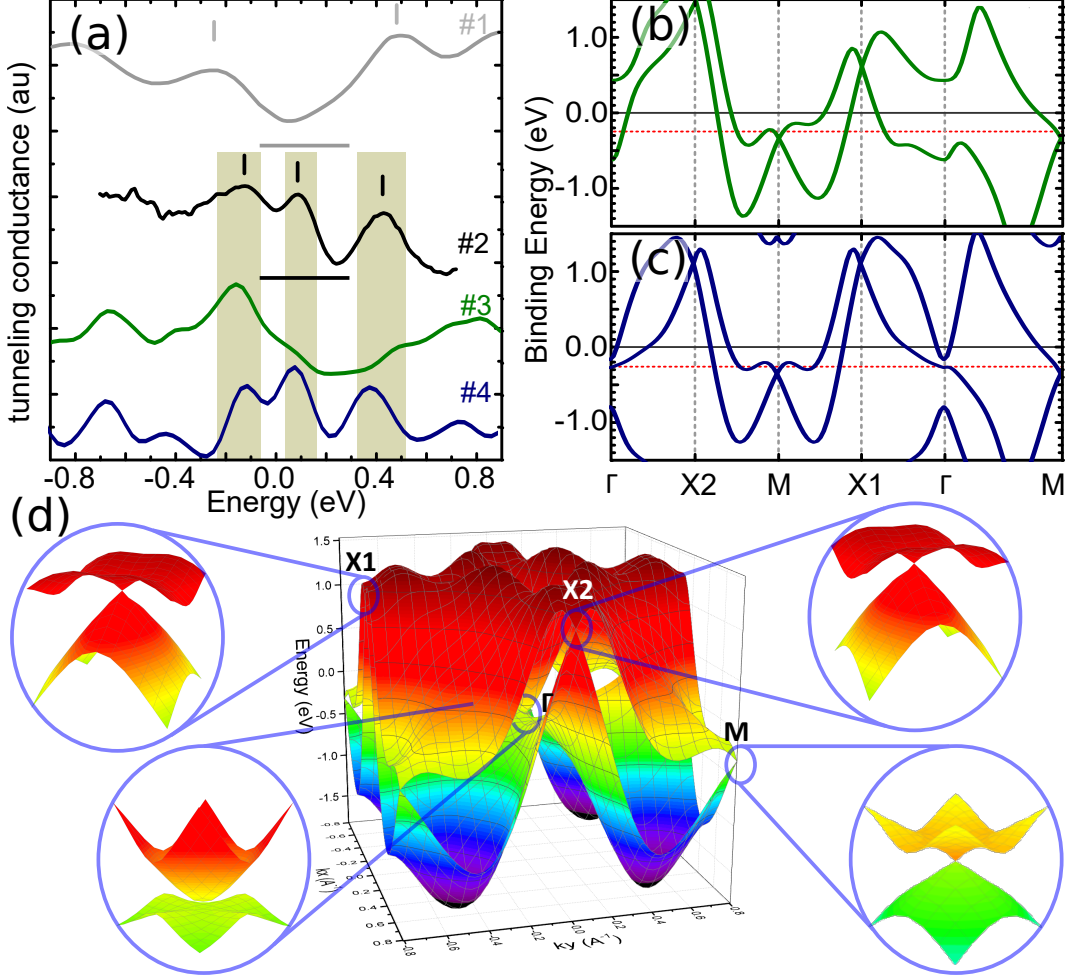


FIG. 4. (a) Tunneling conductance spectra recorded for α -Bi (#1), MBI (#2), together with the DOS calculated using DFT for $0.37 \times 0.41 \text{ nm}^2$ (#3) and $0.39 \times 0.39 \text{ nm}^2$ (#4) unit cells. Shaded rectangles highlight the positions of the three main experimental peaks for MBI. (b) Band diagram for $3.7 \times 4.1 \text{ nm}^2$ and (c) $0.39 \times 0.39 \text{ nm}^2$ unit cells. (d) 3D plot of the band structure shown in (c). The red dotted lines in (b) and (c) indicate the location of the Fermi levels used to shift #3 and #4 in (a) (0.25 eV and 0.28 eV respectively).

151 atomic positions were allowed to relax from the default bulk values by energy minimization
 152 until the Hellmann-Feynman forces were reduced to below $1.0 \times 10^5 \text{ eV/\AA}$. We find that a
 153 single monolayer of α -Bi is not stable – this is expected, because the 2nd layer in the paired
 154 layer structure is required to hold it together. Remarkably, however, we find that a single
 155 monolayer structure with symmetry similar to that of the Bi(110) structure is stable if it is
 156 considerably contracted with respect to that of the Bi(110) structure.

157 We find that the minimum energy structure obtained after full optimization has a unit
 158 cell with dimensions $0.37 \times 0.41 \text{ nm}^2$ (the band structure is shown in Fig. 4(b)). We also
 159 consider a structure that is constrained to have a square unit cell with the dimensions
 160 $0.39 \times 0.39 \text{ nm}^2$ that best match the atomic resolution and moiré measurements discussed
 161 above (band structure shown in Fig. 4(c)). Then our DFT calculations show that the
 162 energy is minimised when the middle atom is located at $(0.47a, 0.5a)$ where $a = 0.39 \text{ nm}$
 163 and is displaced vertically by 0.145 nm (see Fig. 1(c)). The energy of this structure is only
 164 slightly higher (-306.55 versus $-306.58 \text{ eV/unit cell}$) than for the $0.37 \times 0.41 \text{ nm}^2$ structure
 165 but is significantly lower than for the unstable single monolayer of $\alpha\text{-Bi}$ (-306.11 eV/unit
 166 cell). These freestanding monolayer structures all have higher energy than $2\text{ML-}\alpha\text{-Bi}$ ($\frac{1}{2} \times$
 167 $-613.70 \text{ eV/unit cell} = -306.85 \text{ eV/unit cell/ML}$), but we expect that the interaction with
 168 the underlying substrate most probably changes the energy balance and makes the MBI
 169 structures more stable. Unfortunately, it is computationally too expensive to simulate the
 170 whole incommensurate structure, because it requires a very large supercell.

171 Fig. 4(a) shows that the calculated DOS for the $0.39 \times 0.39 \text{ nm}^2$ structure (curve #4) is
 172 in excellent agreement with the experimental STS data (curve #2). The shading highlights
 173 the good agreement in the number of the main peaks in the spectrum, and their positions
 174 after taking into account small shifts in the Fermi level due to doping from the substrate³³
 175 (the precise doping mechanism is unclear and requires further investigation). In contrast,
 176 the calculated DOS for the $0.37 \times 0.41 \text{ nm}^2$ unit cell (#3) does not reproduce all the features
 177 of the experimental data. Taking into consideration the unit cell measured using STM, the
 178 good fit of moiré simulations to the experimentally observed data, and the good agreement
 179 with calculated density of states it is clear that the MBI films grow in the $0.39 \times 0.39 \text{ nm}^2$
 180 structure instead of minimum energy one.

181 The two bands evident in Figs. 4(b) and (c) originate from the unsaturated Bi-6p orbitals
 182 of the two atoms in the unit cell. Of particular interest is the existence of two-dimensional
 183 Dirac cones in the band structure of MBI films (which are in some ways similar to those
 184 observed in topological metals^{34,35}). As shown in Fig. 4(b,c), for both the $0.39 \times 0.39 \text{ nm}^2$ and
 185 $0.37 \times 0.41 \text{ nm}^2$ structures, the two bands cross each other at the M, X1, and X2 points, and
 186 because the bands have opposite parity eigenvalues they form three two-dimensional Dirac
 187 cones. The Dirac points at M, and X2 are protected by the mirror reflection symmetry of
 188 the lattice. However a small energy gap (not visible on this scale) is opened at the Dirac

189 point at X1 because the mirror symmetry is broken by the displacement of the central atom
190 within the unit cell (Fig. 1(c)). Ref. [25] discusses these symmetry issues for Bi films with
191 odd-layer thicknesses in more detail and shows that – in contrast with graphene – the strong
192 spin-orbit coupling in MBi is essential for creating Dirac cones in this system. Therefore, the
193 MBi films realised here a unique opportunity for investigating strongly spin-orbit coupled
194 2D Dirac fermions.

195 The MBi structure reported here is a new allotrope which was neither observed nor
196 predicted previously, and is the first monolayer bismuth structure observed with rectangular
197 symmetry. In its present form the MBi is only observed relatively rarely and appears to
198 rely on nucleation at defects and imperfections in supporting Bi(110) stripe structures,
199 but similar structures might be realized among other materials in 15th group of periodic
200 table and / or by careful choice of alternate substrates. Clearly further work is required to
201 determine whether larger areas of the novel monolayer structure can be obtained by this or
202 other synthesis methods, and microelectronics compatible substrates are required to allow
203 transport measurements that exploit the multiple Dirac cones that are the key features of
204 the band structure.

205 **Acknowledgements.** This work was supported by the National Science Centre, Poland
206 (DEC-2015/17/B/ST3/02362, P.J.K), the Marsden Fund and MacDiarmid Institute for Ad-
207 vanced Materials and Nanotechnology (O.M., and S.A.B.), the National Natural Science
208 Foundation of China (11204133, X.X.W) and the U.S. National Science Foundation (NSF-
209 DMR-1305583, T.-C.C.).

210 **Appendix: Moiré pattern simulation**

211 Our moiré simulations are presented in Fig. 5 below, which compares the modelled period
 212 and rotation angle of the moiré pattern with the experimental values. We have performed
 213 a series of simulations and explored a range of unit cells for the overlayer (including models
 214 both with and without the central atom in the unit cell). We find that an MBI unit cell of
 215 $3.92 \times 3.92 \text{ \AA}^2$ uniquely explains (red symbols) the values of the moiré periodicity and lack
 216 of angular dependence of the moiré pattern. Note that it also explains the second moiré
 217 periodicity (in the orthogonal direction, experimental data point at the top right of Fig. 5).
 218 To demonstrate the exquisite sensitivity of the moiré pattern periodicity to changes in the
 219 MBI unit cell we also show (purple diamonds) the variation of periodicity with rotation
 220 angle for an MBI unit cell of $3.97 \times 3.97 \text{ \AA}^2$. The purple diamonds do not agree well with
 221 the experimental data - evidently the uncertainty in the MBI unit cell dimensions is smaller
 222 than 0.1 \AA .

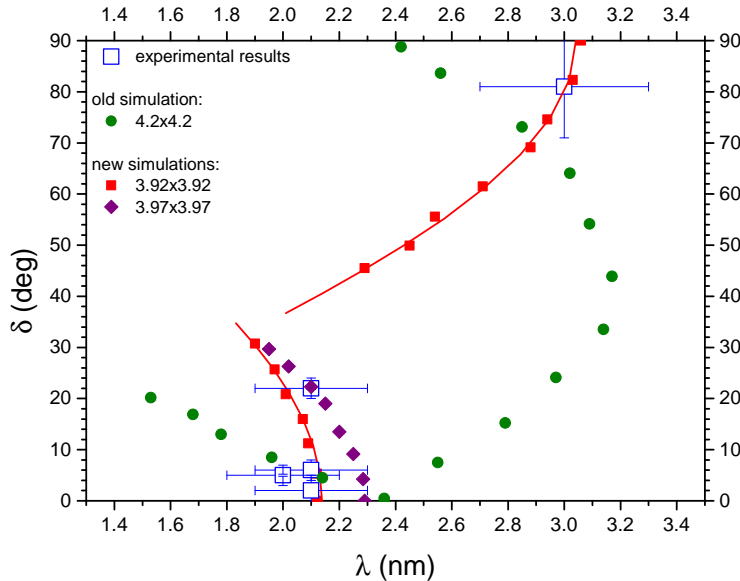


FIG. 5. Angle between moiré pattern and substrate direction, δ , versus moiré periodicity, λ , for experimental data (open squares) and two simulated square unit cells $3.92 \times 3.92 \text{ nm}^2$ (filled squares) and $3.97 \times 3.97 \text{ nm}^2$ (filled diamonds).

-
- 223 * electronic address: pawel.kowalczyk@uni.lodz.pl
- 224 † electronic address: simon.brown@canterbury.ac.nz
- 225 ¹ K. S. Novoselov, A. K. Geim, S. V. Morozov, D. Jiang, M. I. Katsnelson, I. V. Grigorieva, S. V.
226 Dubonos, and A. A. Firsov, *Nature* **438**, 197 (2005).
- 227 ² A. H. Castro Neto, F. Guinea, N. M. R. Peres, K. S. Novoselov, and A. K. Geim, *Rev. Mod.*
228 *Phys.* **81**, 109 (2009).
- 229 ³ A. C. Ferrari, F. Bonaccorso, V. Fal'ko, K. S. Novoselov, *et al.*, *Nanoscale* **7**, 4598 (2015).
- 230 ⁴ A. J. Mannix, B. Kiraly, M. C. Hersam, and N. P. Guisinger, *Nat. Rev. Chem.* **1**, 0014 (2017).
- 231 ⁵ A. Kara, H. Enriquez, A. P. Seitsonen, L. L. Y. Voon, S. Vizzini, B. Aufray, and H. Oughaddou,
232 *Surf. Sci. Rep.* **67**, 1 (2012).
- 233 ⁶ M. E. Dávila, L. Xian, S. Cahangirov, A. Rubio, and G. L. Lay, *New J. Phys.* **16**, 095002
234 (2014).
- 235 ⁷ E. Bianco, S. Butler, S. Jiang, O. D. Restrepo, W. Windl, and J. E. Goldberger, *ACS Nano* **7**,
236 4414 (2013).
- 237 ⁸ K. S. Novoselov, D. Jiang, F. Schedin, T. J. Booth, V. V. Khotkevich, S. V. Morozov, and
238 A. K. Geim, *Proc. Natl. Acad. Sci. U. S. A.* **102**, 10451 (2005).
- 239 ⁹ B. Radisavljevic, A. Radenovic, J. Brivio, V. Giacometti, and A. Kis, *Nature Nano.* **6**, 147
240 (2011).
- 241 ¹⁰ H. S. S. Ramakrishna Matte, A. Gomathi, A. K. Manna, D. J. Late, R. Datta, S. K. Pati, and
242 C. Rao, *Angew. Chem.* **122**, 4153 (2010).
- 243 ¹¹ Z. Zeng, Z. Yin, X. Huang, H. Li, Q. He, G. Lu, F. Boey, and H. Zhang, *Angew. Chem. Int.*
244 *Ed.* **50**, 11093 (2011).
- 245 ¹² L. Li, Y. Yu, G. J. Ye, Q. Ge, X. Ou, H. Wu, D. Feng, X. H. Chen, and Y. Zhang, *Nat. Nano.*
246 **9**, 372 (2014).
- 247 ¹³ J. Wood, S. Wells, D. Jariwala, K.-S. Chen, E. Cho, V. Sangwan, X. Liu, L. J. Lauhon, T. Marks,
248 and M. Hersam, *Nano Lett.* **14**, 6964 (2014).
- 249 ¹⁴ O. Osters, T. Nilges, F. Bachhuber, F. Pielhofer, R. Wehrich, M. Schöneich, and P. Schmidt,
250 *Angew. Chem. Int. Ed.* **51**, 2994 (2012).
- 251 ¹⁵ Z. F. Wang, L. Chen, and F. Liu, *Nano Lett.* **14**, 2879 (2014).

- 252 ¹⁶ S. Zhang, M. Xie, F. Li, . Yan, Y. Li, E. Kan, W. Liu, Z. Chen, and H. Zeng, *Angew. Chem.*
253 *Int. Ed.* **55**, 1666 (2016).
- 254 ¹⁷ T. Nagao, J. T. Sadowski, M. Saito, S. Yaginuma, Y. Fujikawa, T. Kogure, T. Ohno,
255 Y. Hasegawa, S. Hasegawa, and T. Sakurai, *Phys. Rev. Lett.* **93**, 105501 (2004).
- 256 ¹⁸ P. J. Kowalczyk, D. Belic, O. Mahapatra, S. A. Brown, E. S. Kadantsev, T. K. Woo, B. Ingham,
257 and W. Kozlowski, *Appl. Phys. Lett.* **100**, 151904 (2012).
- 258 ¹⁹ P. J. Kowalczyk, O. Mahapatra, S. A. Brown, G. Bian, X. Wang, and T.-C. Chiang, *Nano*
259 *Lett.* **13**, 43 (2013).
- 260 ²⁰ G. Wang, R. Pandey, and S. P. Karna, *ACS Appl. Mater. Interfaces* **7**, 11490 (2015).
- 261 ²¹ M. Wada, S. Murakami, F. Freimuth, and G. Bihlmayer, *Phys. Rev. B* **83**, 121310 (2011).
- 262 ²² Y. Lu, W. Xu, M. Zeng, G. Yao, L. Shen, *et al.*, *Nano Lett.* **15**, 80 (2015).
- 263 ²³ S. A. Scott, M. V. Kral, and S. A. Brown, *Phys. Rev. B* **72**, 205423 (2005).
- 264 ²⁴ G. Bian, T. Miller, and T.-C. Chiang, *Phys. Rev. B* **80**, 245407 (2009).
- 265 ²⁵ G. Bian, X. Wang, T. Miller, T.-C. Chiang, P. J. Kowalczyk, O. Mahapatra, and S. A. Brown,
266 *Phys. Rev. B* **90**, 195409 (2014).
- 267 ²⁶ S. A. Scott, M. V. Kral, and S. A. Brown, *Phys. Rev. B* **73**, 205424 (2006).
- 268 ²⁷ D. N. McCarthy, D. Robertson, P. J. Kowalczyk, and S. A. Brown, *Surf. Sci.* **604**, 1273 (2010).
- 269 ²⁸ P. J. Kowalczyk, O. Mahapatra, D. N. McCarthy, W. Kozlowski, Z. Klusek, and S. A. Brown,
270 *Surf. Sci.* **605**, 659 (2011).
- 271 ²⁹ P. J. Kowalczyk, D. Belić, O. Mahapatra, and S. A. Brown, *Acta Mater.* **60**, 674 (2012).
- 272 ³⁰ P. J. Kowalczyk, O. Mahapatra, D. Belić, S. A. Brown, G. Bian, and T.-C. Chiang, *Phys. Rev.*
273 *B* **91**, 045434 (2015).
- 274 ³¹ P. Hofmann, *Prog. Surf. Sci.* **81**, 191 (2006).
- 275 ³² D. A. Cosma, J. R. Wallbank, V. Cheianov, and V. I. Fal'ko, *Faraday Discuss.* **173**, 137 (2014).
- 276 ³³ I. Gierz, C. Riedl, U. Starke, C. R. Ast, and K. Kern, *Nano Lett.* **8**, 4603 (2008).
- 277 ³⁴ H. Ji, I. Pletikosić, Q. D. Gibson, G. Sahasrabudhe, T. Valla, and R. J. Cava, *Phys. Rev. B*
278 **93**, 045315 (2016).
- 279 ³⁵ J. Nayak, S.-C. Wu, N. Kumar, C. Shekhar, S. Singh, J. Fink, E. E. D. Rienks, G. H. Fecher,
280 S. S. P. Parkin, B. Yan, and C. Felser, *Nat. Commun.* **8**, 13942 (2017).